Investigation of snow sintering at microstructural scale from micro-penetration tests

Isabel Peinke, Pascal Hagenmuller, Guillaume Chambon, Jacques Roulle

Version of Record: https://www.sciencedirect.com/science/article/pii/S0165232X18305275
Manuscript_e988e3723b009b6cd1787ca40a9c5d3f

Investigation of snow sintering at microstructural scale from micro-penetration tests

Isabel Peinke[a,*], Pascal Hagenmuller[a], Guillaume Chambon[b], Jacques Roulle[a]

[a] *Univ. Grenoble Alpes, Université de Toulouse, Météo-France, CNRS, CNRM, Centre d'Études de la Neige, Grenoble, France*
[b] *Univ. Grenoble Alpes, IRSTEA, UR ETGR Erosion Torrentielle, Neige et Avalanches, Grenoble, France*

Abstract

Snow sintering is investigated at microscopic and macroscopic scales with high-resolution cone penetration tests. In a cold room at -10°C, vertical profiles of penetration force were measured periodically during 24 hours using the SnowMicroPenetrometer in four snow samples, which differed only by their grain sizes. We estimated the evolution of snow micromechanical properties, namely the bond rupture force, the deflection at rupture and the number of ruptures per penetration increment, by applying a statistical analysis to penetration profiles. The upper part of the profiles is transient due to the progressive formation of a compaction zone in front of the cone tip. In order to explicitly account for this process in the statistical analysis, we used a non-homogeneous Poisson shot noise model which considers a depth dependency of the rupture occurrence rate. On simulated transient profiles, this analysis is shown to provide accurate estimates of the micromechanical properties. On our experimental data, the method effectively revealed that the vertical heterogeneity of penetration force was essentially due to variations of the rupture rate. Conversely, the time evolution of the macroscopic force was mainly due to microstructural bond strengthening. Both macroscopic force and bond rupture force followed a power law with an average exponent of 0.27 and 0.29, respectively. On our samples, a higher exponent for larger grains was observed on the microscopic bond force, while no trend with grain size was visible in the exponent characterizing the macroscopic force evolution.

*Corresponding author
Email address: isabel.peinke@meteo.fr (Isabel Peinke)

Keywords: snow, sintering, penetration tests, mechanical properties, snow microstructure

1. Introduction

Snow on Earth exists at a relative high homologous temperature. Once deposited on the ground, snow thus remains very active thermodynamically and its structure changes continuously. One process of this metamorphism is sintering, i.e. the creation and growth of bonds between snow particles [1]. The sintering has long been recognized to significantly affect the evolution of snow mechanical properties, generally in the form of a progressive strengthening of the material [2, 3], and manifests over a wide range of time scales: from sub-second sintering (e.g. for cornice formation [4]) to hourly time scales (e.g. for fracture healing [5]), to weekly-monthly time scales (e.g. for seasonal snowpack evolution [6]), and up to centuries (e.g. for the formation of glaciers and ice sheets, [7]) . Sintering thus plays an important role, for instance, in avalanche formation [5, 8], in snow management practices such as grooming in ski resorts [9], or in building an igloo.

Sintering is driven by the reduction of surface energy and, depending on environmental conditions, can involve different mechanisms: viscous flow, plastic flow, evaporation, condensation, volume diffusion, and surface diffusion [e.g. 10]. The first studies to identify the driving mechanisms of sintering were conducted in metallurgic powders [e.g. 11, 10]. Kuczynski [10] decomposed the neck growth between metallic particles into different processes and modeled the neck size evolution as a power-law:

$$\left(\frac{r_b}{r_g}\right)^n = \frac{F(T)}{r_g^{n-m}} t \tag{1}$$

where r_g denotes the particle radius, r_b is the neck radius, and $F(T)$ is a temperature dependent parameter. The exponents n and m depend on the active sintering process: $(n = 2,\ m = 1)$ for viscous or plastic flow, $(n = 3,\ m = 2)$ for evaporation and condensation, $(n = 5,\ m = 3)$ for volume diffusion and $(n = 7,\ m = 4)$ for surface diffusion. This formalism was then used to understand the neck growth between ice spheres [e.g. 12, 13, 14]. Hobbs and Mason [14] considered that Kucynzski's model was not directly applicable to ice, particularly for vapour transport. Applied to ice, they found values of $n = 5$ and $m = 3$ in Eq. 1 for the sintering process corresponding to vapour transport. In

their experiments on ice spheres of diameters between 50 and 700 μm and at temperatures between -3 and -20°C, they also found that the dominant mechanism for ice sintering is evaporation-condensation and that the diffusion process plays only a minor role. Maeno and Ebinuma [15] revisited the different mechanisms contributing to ice neck growth and concluded that vapour transport from a surface source is the major mechanism in most natural and laboratory conditions, while surface diffusion dominates only for small neck radii and either high (> 0.95) or low (< 0.85) homologous temperatures. Chen and Baker [16] showed on high resolution images that the evolution of a neck between two ice spheres is primarily due to the direction and rate of water vapour transport. In addition to grain size and temperature dependence, sintering mechanisms in snow were also shown to be controlled by contact pressure and grain shape [e.g. 17, 1].

While previous studies have provided valuable insight into the physics of snow sintering in simplified geometries, namely ice spheres, quantitative data on natural snow sintering remained rather scarce, as recalled by [18, 19]. Indeed, many studies have investigated the general evolution of the snow microstructure with time under different temperature and loading conditions [e.g. 20, 21, 22, 23] but only a few ones have focused on the specific evolution of bond size without any other changes of the microstructure (e.g. grain shape evolution, settlement). Ramseier and Sander [24] measured the influence of temperature on the strengthening of natural snow with mechanical compression tests. They observed faster strengthening in compression for higher temperature. Similarly, Matsushita et al. [25] observed a more active sintering with higher snow temperatures and higher normal loads caused by overlying snow. Montmollin [26] observed a regeneration of destroyed bonds under shear deformation for low deformation rates, which highlights the competition between bond re-welding by sintering and bond failure during deformation. Herwijnen and Miller [19] used a SnowMicroPenetrometer (SMP, [27]) to measure sintering through the time-evolution of the penetration force in different snow types (for times up to $5 - 8$ hours). Podolskiy et al. [28] developed mechanical shear tests to investigate the effect of isothermal sintering on interface strengthening at various normal pressures. These latter authors [19, 28] proposed to represent the time-evolution of macroscopic force or strength as a power-law:

$$F(t) = F(t = t_0) \left(\frac{t}{t_0} \right)^{\alpha_F} \tag{2}$$

with F the force or strength, t the time and α_F a sintering exponent. Typical sintering exponents for seasonal snow are reported in the range between 0.07 and 0.36, as reviewed by Podolskiy et al. [28]. In their experiments, Podolskiy et al. [28] measured an average exponent of 0.21±0.08, and observed that higher pressures applied during sintering tend to increase this exponent. Herwijnen and Miller [19] derived a mean sintering exponent of 0.18±0.05, and observed lower sintering rates for low-density snow (consisting mostly of dendritic grain morphologies) compared to higher density snow. They hypothesize that this relation is the result of two competing processes: (1) bond creation and growth and (2) bond vanishing due to the metamorphism of dendritic forms into compact rounded particles. In parallel, they simulated the microscopic bond-to-grain ratio for simplified spherical ice grains and observed a power-law growth with the same average exponent as that derived from the experiments. Based on this agreement, they suggest that the mean macroscopic penetration resistance closely relates to the microscopic bond-to-grain ratio in snow.

In spite of the advances described above, direct and concurrent measurements of sintering exponents at both microscopic and macroscopic scales in snow, are still lacking. Accordingly, the precise relation between bond growth, at the microscopic scale, and increase in mechanical strength or resistance at the macroscopic scale, largely remains to be elucidated. In this study, we use micro-cone penetration tests (μCPT) to investigate snow sintering at both macroscopic and microscopic scales. Here, the microscopic scale corresponds to the grain scale of about tenths of millimeters and the macroscopic scale corresponds to the sample scale of about a few centimeters. μCPT measurements were conducted with a modified SMP on thin snow samples during 24 hours after snow sieving in a cold room at -10°C. In parallel to the macroscopic penetration force, micromechanical properties, including the bond rupture force, are estimated through an extension of the shot noise model introduced for snow by Löwe and Herwijnen [29]. In the first section, we present the experimental setup and models required to derive micromechanical properties from the penetration profiles. The models are first evaluated on simulated penetration profiles. The penetration profiles measured on the samples evolving with sintering are then analyzed at the macroscopic and microscopic scales. Finally, the outcomes in terms of μCPT processing techniques and knowledge on snow sintering are discussed.

Table 1: Physical properties of the snow samples used in this study.

Sample name	Snow type	Sieve size (mm)	Grain size (mm)	SSA (m^2 kg^{-1})	Density (kg m^{-3})
SSA18a	RGlr	0.8	0.7	17.9±0.3	500±2
SSA18b	RGlr	0.8	0.7	17.9±0.3	500±2
SSA14	RGlr	1.0	0.9	14.0±0.3	496±2
SSA10	RGlr	1.6	1.5	10.4±0.1	484±3

2. Material and Methods

2.1. Snow samples

We prepared four snow samples with a snow type characterized as large rounded grains (RGlr, Fierz et al. [30]). The samples were prepared at a controlled temperature of -10±0.5°C by sieving about 35 mm height of snow into rectangular boxes of size 300 x 400 mm. In order to get samples with different grain sizes, the rounded grains were sieved using various sieve sizes (Tab. 1). Two samples with a sieve size of 0.8 mm (samples SSA18a and SSA18b) one sample with a sieve size of 1.0 mm (sample SSA14), and one sample with a sieve size of 1.6 mm (sample SSA10) were prepared. The samples showed densities of about 500 kg m^{-3}, grain sizes between 0.7 and 1.5 mm and specific surface areas (SSA) ranging between 10 and 18 m^2 kg^{-1}. Density was measured by weighing 50 cm^3 sub-samples extracted with a cutter. SSA was measured using an optical method (DUFISSS, Gallet et al. [31]) at different heights and different horizontal locations to characterize spatial variability. The vertical variability of SSA was found of the same order as the horizontal one (typically, the standard deviations were less than 1 m^2 kg^{-1}). Grain size was estimated with microscope images (magnification by a factor of 32) of the grains.

2.2. Micro-penetration tests in sintering snow

In the following 24 hours after the sieving, a total of 31 micro-cone penetration tests (μCPT) (4 to 5 measurements for 7 different times) were conducted in each sample. This high number of measurements enables to take into account the spatial variability of the sample due to the sieving procedure [e.g. 19]. To avoid interference in neighboring

penetration tests, we kept a distance of 40 mm between the measurements. To avoid effects of the lateral walls, no measurement were performed closer than 40 mm to the walls.

The μCPTs in this study were conducted with a modified version of the SnowMicroPenetrometer (SMP version 4, [27]). The SMP is a high-resolution penetrometer, which consists of a conical tip with a 60° apex angle and a maximum diameter of 5 mm, driven into the snow by a motor with a constant speed of 20 mm s^{-1}. The depth and force sensors record measurement points at a sampling frequency of 5 kHz, i.e. every 4 μm penetration increment. The SMP measures the snow resisting force applied to the cone tip only and not to the rod. The modification of the SMP for this study consisted in lengthening the apex by 40 mm (Fig. 1). This lengthening of the apex was motivated to prevent the rod of the SMP to penetrate in the sample, and thus influence the measured force through the formation of a rod-induced compaction zone (CZ). LeBaron et al. [32] measured the CZs around a split-axis SMP probe that has the same geometry as the SMP (tip and rod), and found significantly larger CZs than in the study of Herwijnen [33], who analyzed of the CZ around the SMP tip without the rod. Given the size of our snow samples, we wanted to avoid any potential impact of the rod, and account only for the CZ due to the tip. Note that side-by-side measurements performed with the original and modified SMP versions showed essentially identical penetration profiles, as long as the rod of the original SMP does not touch snow (Appendix A).

As a typical example, Figure 2 shows μCPT profiles measured after a rest time of 24 hours on sample SSA18a. Single profiles present high frequency fluctuations and large vertical variations (Fig. 2a). Even though the sieving procedure may induce a limited vertical heterogeneity of the snow sample [e.g. 19], vertical profiles of SSA did not reveal any significant vertical variations (standard deviations were less than 1 m^2 kg^{-1}). Based on the study of Podolskiy et al. [28], we can also argue that pressure exerted by overburden snow is unlikely to explain this vertical heterogeneity. The overburden pressure at a depth of 35 mm was estimated about 0.2 kPa, and these authors showed no significant increase of the sintering rate for normal loads lower than 0.5 kPa.

We thus argue that the vertical heterogeneity in the μCPT profiles is mainly caused by the interaction between the snow and the μCPT tip. The increase of the penetration

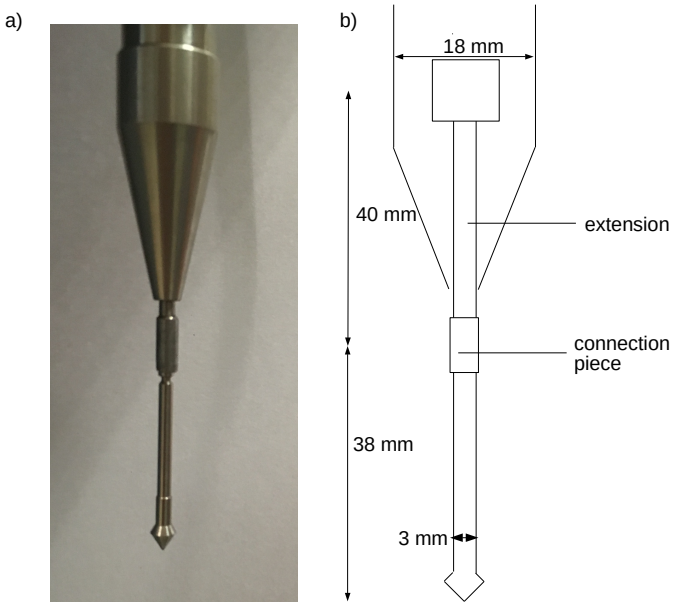

Figure 1: Experimental setup: (a) photo and (b) scheme of the modified tip.

force up to a depth of about 5 mm is due to the progressive penetration of the conic apex into the sample. The increase of force for depths between 5 and 25 mm is then probably caused by the progressive formation of the CZ in front of the tip. According to Herwijnen [33], the full development of the tip-induced CZ is reached after 40 mm penetration depth, and therefore probably not reached in our experiments. Finally, the decrease of force for depths larger than 25 mm is presumably due to the influence of the rigid bottom of the sample box. Penetration profiles shown by Herwijnen and Miller [19] also exhibited a maximum force a few centimeter above the sample holder bottom. In the following analyses, to avoid this artifact caused by sample bottom, we will only account for the first 25 mm of the penetration profiles.

Figure 2b shows four smoothed μCPT profiles measured in the same box and at the same time. Slight differences between the profiles are visible. This horizontal heterogeneity in the samples remains comprised between 10 and 15% (relative horizontal standard deviation), and is probably due to the sieving.

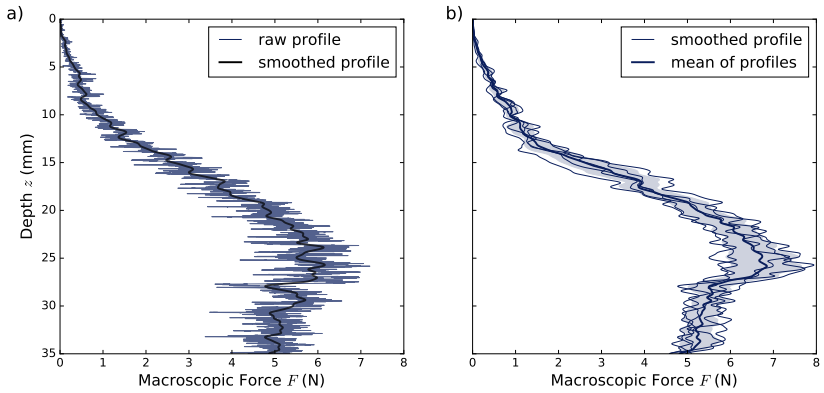

Figure 2: Examples of μCPT profiles measured on sample SSA18a after a rest time of 24 h: (a) one raw profile and the corresponding smoothed profile (black), (b) four smoothed μCPT profiles measured at different positions. The profiles were smoothed with a Gaussian filter with a standard deviation of 0.2 mm. The mean of the four smoothed profiles is also shown (bold line), and its standard deviation represented as the shaded area.

2.3. Micromechanical analysis methods

Several statistical models were proposed to interpret SMP profiles in terms of micromechanical property proxies. Johnson and Schneebeli [34] assumed that the penetration force profile results from the superposition of spatially uncorrelated ruptures. Marshall and Johnson [35] extended this theory by using Monte-Carlo simulations to take into account simultaneous rupture events and inverted the signal. Löwe and Herwijnen [29] adapted the model into the formalism of a homogeneous Poisson point process (HPP), such that individual ruptures can overlap and are randomly distributed.

All these models interpret a SMP profile $F(z)$, i.e. the macroscopic penetration force F as a function of depth z, as the superposition of spatially uncorrelated rupture events (Fig. 3). Each single event corresponds to the rupture of one bond behaving in an elastic-brittle manner. These events are assumed to be identical, but to occur at random depths. They are described by two microstructural properties, namely the deflection length δ and the rupture force f, and express as $f_z(z) = f/\delta \times \theta(z) \times \theta(\delta - z)$ with θ the Heaviside function (Fig. 3 inset). The number of events occurring per penetration increment is described by a Poisson distribution with an intensity λ_z. The convolution of the single event function f_z and a random sampling of the number of events results in a simulated

profile $F(z)$ (Fig. 3).

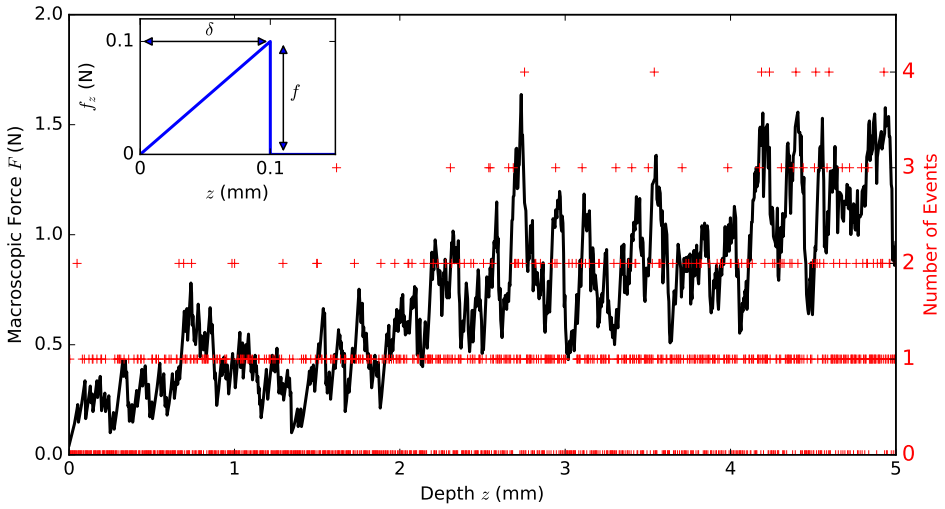

Figure 3: Simulated force penetration profile obtained as the superposition of uniform elastic brittle events (inset) whose number of occurrence follows a homogeneous Poisson distribution. Here, δ=0.1 mm, f=0.1 N, and λ_z is linear increasing with depth: $\lambda_z(z) = a_\lambda z + b_\lambda$ with $a_\lambda = 40$ mm^{-2} and $b_\lambda = 50$ mm^{-1}.

Homogeneous Poisson process (HPP)

Assuming that the intensity λ_z is constant over depth and equal to λ, Löwe and Herwijnen [29] derived analytical expressions directly linking the stochastic cumulants and correlation function of the SMP profile F to the micromechanical properties δ, f and λ. In particular, they obtained the following relations:

$$\kappa_n(z) = \frac{f^n \delta \lambda}{n+1} \quad \text{and} \quad C(z, z+r, |r| < \delta) = f^2 \delta \lambda \left(\frac{1}{3} - \frac{1}{2}\frac{|r|}{\delta} + \frac{1}{6}\frac{|r|^3}{\delta^3} \right) \tag{3}$$

where κ_n is the cumulant of order n (e.g. κ_1 is the mean, κ_2 is the variance) and C is the two-point correlation function. This process with a constant intensity $\lambda_z(z) = \lambda$, is called henceforth homogeneous Poisson process (HPP). Note that the formalism of the Poisson processes implies constant event characteristics, i.e. δ and f are constant (or in a constant distribution). The assumption of a constant intensity also implies stationarity of $F(z)$, and thus enables to compute the stochastic cumulants and correlation function as "depth" cumulants and correlation function (ergodicity). In practice however, measured penetration profiles are rarely stationary with depth even for homogeneous snow layers

[19]. This difficulty is overcome by splitting the profile in smaller windows where the assumption of stationarity remains valid [e.g. 36]. It is observed on simulated HPPs that better results are obtained with larger windows [29]. Therefore, a balance between large windows that are stochastically representative, and small windows on which the profile can be considered stationary, needs to be found. Typical window sizes Δz of 1 to 5 mm are reported in the literature [e.g. 29, 36, 37]. Note that, in practice, the correlation function C is also generally computed on detrended profiles (i.e. the mean and linear trend are subtracted on each window) [e.g., 29, although not shown therein].

Non-homogeneous Poisson process (NHPP)

As shown in Fig. 2, the penetration force measured in our experiments displays strong changes with depth. The profiles were limited to a depth of 35 mm due to the modified design of the SMP tip. As explained in Sect. 2.2, the snow structure exhibited a rather homogeneous vertical profile. We can thus reasonably assume that the microstructural properties δ and f are constant over the entire depth, while only the number of events, thus the intensity λ_z, varies with depth. This depth variation of λ_z can be related to the build-up of the compaction zone in front of the tip. We thus propose to analyze our measured μCPT profiles as a non-homogeneous Poisson process (NHPP), with a variable intensity λ_z, instead of a homogeneous Poisson process (HPP). Note that the NHPP equals to the HPP if λ_z is constant with depth.

We describe here the main steps of the mathematical developments. Details can be found in Appendix B. Let us consider $F(z)$ as a NHPP characterized by an elastic brittle event f_z, whose properties f and δ are assumed to be constant with depth and a number of events in a Poisson distribution of intensity $\lambda_z(z)$. Assuming that the relative variations of $\lambda_z(z)$ over an interval of length δ are negligible, it can be shown that:

$$\kappa_n(z) = \frac{f^n \delta \lambda_z(z)}{n+1} \quad \text{and} \quad C(z, z+r, |r| < \delta) = f^2 \delta \lambda_z(z) \left(\frac{1}{3} - \frac{1}{2}\frac{|r|}{\delta} + \frac{1}{6}\frac{|r|^3}{\delta^3} \right). \tag{4}$$

Equation (4) is identical to Eq. (3) obtained by Löwe and Herwijnen [29], but with $\lambda_z(z)$ instead of a constant intensity λ. However, F cannot anymore be assumed stationary, and therefore its cumulants and correlation function cannot be computed directly from a single force profile $F(z)$. We thus define $\widetilde{F}$ as:

$$\widetilde{F} = \frac{F - \kappa_1(F)}{\kappa_1(F)^{1/2}} \tag{5}$$

From Eq. (4), it can be shown that $\widetilde{F}$ is stationary and we obtain:

$$f = \frac{3}{2}\overline{\widetilde{F}^2}, \qquad \delta = -\frac{3}{2}\frac{C(0)}{C'(0)}, \qquad \lambda_z(z) = \frac{4}{3\delta}\frac{\kappa_1(F)}{\overline{\widetilde{F}^2}} \tag{6}$$

where $\overline{\bullet}$ denotes the mean over depth. The cumulant $\kappa_1(F)$ appearing in Eq. (6) is the stochastic mean of the NHPP. To compute this quantity from our data, we approximate $\kappa_1(F)$ by the "depth" mean $\overline{F}$ calculated on a running window of width Δz=3 mm and on a single profile. Since $\kappa_1(F)$ is a first order cumulant, this approximation is relatively robust, and even exact if the intensity λ_z is linear over intervals of width Δz.

3. Results

3.1. Evaluation of the μCPT analysis method

In this section, we compare the proposed NHPP analysis and the original HPP analysis both on simulated penetration profiles with known properties, and on the μCPT profiles measured in this study.

3.1.1. Evaluation on simulated profiles

First, we evaluated the models on profiles produced by the simulation of a non homogeneous Poisson process. A linearly evolving intensity $\lambda_z(z) = a_\lambda z + b_\lambda$ was considered. The simulated profiles have a length of 25 mm and a resolution of 4 μm, with prescribed parameters (see legend of Fig. 4) similar to the micromechanical properties of our samples. To analyze the influence of the different parameters (f, δ, and a_λ), we performed a sensitivity analysis by varying one parameter within a certain range while keeping the others constant. For each set of parameters, 500 independent profiles were simulated. Since the intensity $\lambda_z(z)$ varies with depth, we defined $\overline{\lambda}$ as its mean over the whole depth to provide a single scalar in the sensitivity analysis. The value $\overline{\lambda}$ was varied by varying a_λ in the range [0, 300] mm^{-2}, while b_λ was kept constant at 50 mm^{-1}. Moreover, three different analysis window sizes Δz of 1, 3 and 10 mm were tested.

Both methods provide similar estimates of the deflection at rupture δ with a root mean square error (RMSE) of 0.59 mm for the HPP and 0.54 mm for the NHPP (Figs. 4a,b). Note that large values of δ tend to be underestimated by the two analyses. Nonetheless, this parameter is correctly estimated if the analysis window is sufficiently large (Δz =

10 mm), especially with the NHPP. Overall, estimates of the microscopic rupture force f are more accurate with the NHPP method with a RMSE of 0.263 N for the HPP and 0.051 N for the NHPP (Figs. 4c,d). As expected, for profiles with an almost constant intensity (a_λ=1 mm^{-2}), the two models provide similar results: a slight underestimation of f. For profiles with a significant evolution of $\lambda_z(z)$ (a_λ=10 or 40 mm^{-2}), the HPP provides accurate estimates of f only for small window sizes, while the NHPP provides accurate estimates for all window sizes. Lastly, the NHPP produces in general a better estimation of the mean intensity $\overline{\lambda}$ (RMSE of 1305 mm^{-1}) than the HPP (RMSE of 2885 mm^{-1}) (Figs. 4e,f). The HPP provides correct estimates of $\overline{\lambda}$ only for large windows and very small values of a_λ, while the NHPP provides correct estimates for all tests. Note that the NHPP tends to slightly overestimate the mean intensity, especially for samples with a large δ and small window sizes.

We can thus conclude that, on non-stationary profiles with an intensity linearly increasing with depth, the NHPP analysis performs better than the HPP analysis in recovering the micromechanical properties. Larger analysis window sizes generally improve the results, especially when the deflection at rupture δ is large. As expected, on almost stationary profiles both methods show similar results.

3.1.2. Comparison on measured profiles

In this section, we compare the two analysis methods on real μCPT profiles. Figure 5 shows the micromechanical properties estimated on the μCPT profiles measured after a rest time of 24 hours as derived from the HPP and NHPP models.

As explained in Section 2.3, with the HPP model, δ, f and λ are assumed constant over small windows of size Δz=3 mm and were computed according to Eqs. (11) and (12) in [29]. With the NHPP model, δ and f are assumed constant over the whole profile, while λ_z can vary with z, and were computed according to Eq. (6). Therefore, the vertical resolutions of the computed micromechanical properties are, by construction, different for the two models.

The HPP analysis shows non-monotonic variations of f with depth (Fig. 5a). It indicates an increase of δ with depth, especially for sample SSA10 characterized by large grains (Fig. 5b). Lastly, an overall increase of λ with depth is observed, with a slight decrease between 10 and 15 mm depth (Fig. 5c). This decrease might be due to the

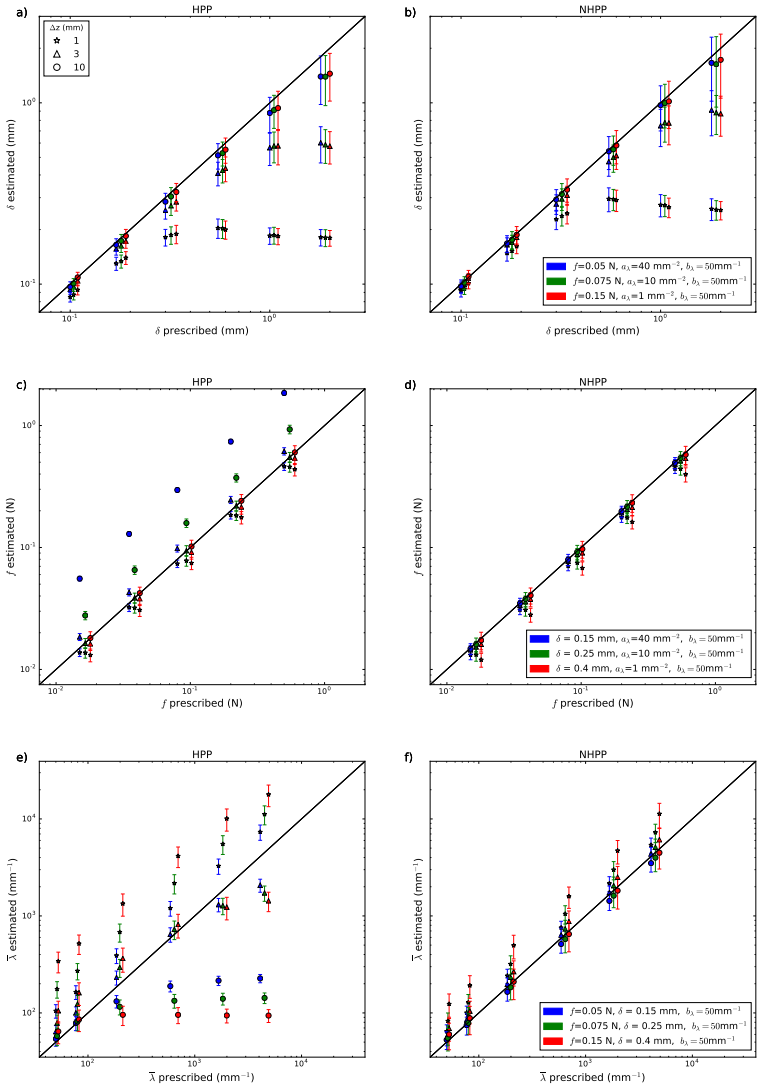

Figure 4: Comparison of estimated and prescribed micromechanical properties δ, f, $\overline{\lambda}$ on simulated penetration profiles. The results of the HPP analysis are shown in (a, c, e), while the results of the NHPP analysis are shown in (b, d, f). In each plot, the values of the constant micromechanical properties, chosen to be similar to those of the samples presented in this study (SSA10 in red, SSA14 in green and SSA18a,b in blue), are indicated in legend. The three different symbols denote the different window sizes Δz. Error bars correspond to the standard deviation over the 500 independent profile realizations.

rapid increase of the macroscopic force F with z in this depth interval (Fig. 2), for which the HPP analysis is not well-designed. Globally, the three parameters follow the overall

increasing trend with depth exhibited in the μCPT force profiles. The HPP analysis distinguishes the different samples on δ and λ, but computes a similar value of f for all samples and almost all depths.

The NHPP analysis distinguishes the different samples on all properties: the largest grains exhibit the largest values of f and δ, and the smallest values of λ. In particular, a noticeable difference between the two analyses is visible on the computed values of f (Figs. 5a,d): unlike the HPP analysis, the NHPP analysis shows a high dependency of f on the different samples. The values of λ_z are found to strictly increase with z, which is consistent with the progressive formation of the compaction zone around the μCPT tip (Fig. 5f). The differences between the two methods become smaller for depths between 20 and 25 mm.

Note that, here, no reference profile of the micromechanical properties is available to definitely evaluate the two models. However, the monotonic increase of intensity with depth, and the the increase of f with grain size, which are only visible in the NHPP estimates, seem more consistent with our knowledge of the sample properties (see Sect. 2.1) and of the progressive formation of the compaction zone [33]. Indeed, Eq. (1) indicates a higher bond size for larger grains and thus an increase of f with grain size can be expected.

3.2. Evolution of the macroscopic force with time

The macroscopic force F clearly increases with time due to sintering (see Fig. 6 or Fig. C.11). Moreover, the relative increase of F with time also appears to be enhanced with depth. For instance, F increases by a factor of about 1.5 over 24 hours at a depth of 5 mm, while it increases by a factor of about 3 at a depth of 20 mm.

In line with previous studies [e.g. 19, 28], the time evolution of the depth-averaged macroscopic force $\bar{F}$ (Fig. 7), was approximated by fitting power laws of the form:

$$\overline{F}(t) = F_{1h} \left(\frac{t}{t_{1h}} \right)^{\alpha_F}, \tag{7}$$

with $t_{1h} = 1$ hour and F_{1h} is the mean macroscopic force value after 1 hour of sintering. $\bar{F}(t)$ is computed as the mean between 0 and 25 mm depth, to exclude any potential influence of the bottom of the box (see Sect. 2.1). The start time $t = 0$ is defined as the middle of the sieving procedure, which took between 5 and 10 minutes. Hence, the error

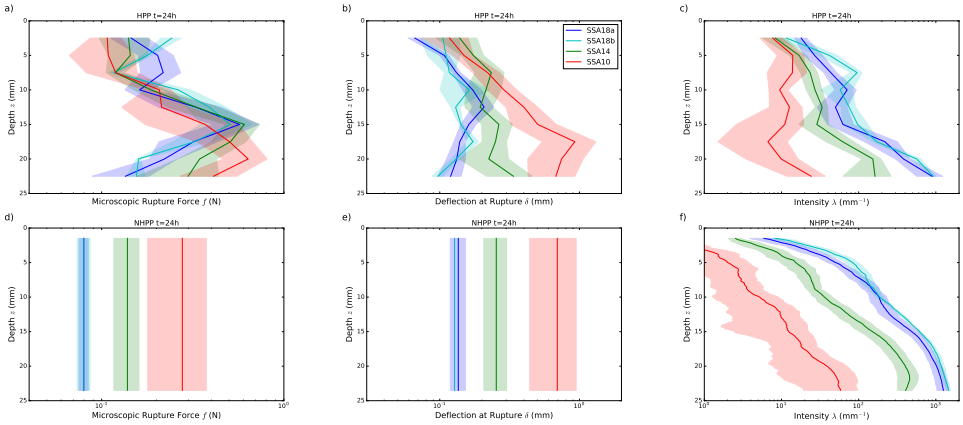

Figure 5: Estimated micromechanical properties derived from the μCPT profiles measured on the samples after a rest time of 24 hours: (a, c) microscopic rupture force f, (b, d) deflection at rupture δ, and (e, f) intensity λ_z, as computed by the HPP (a, b, c) and NHPP (d, e, f) models. The shaded area around the curves represents the standard deviation of the values obtained for the different profiles measured at one sampling time.

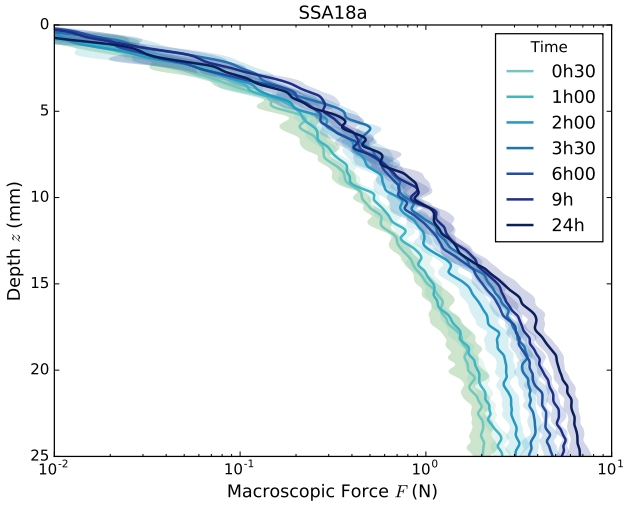

Figure 6: Vertical profile of the macroscopic force F for different sintering times, measured on sample SSA18a.

on sintering time is estimated to be half of the sieving time. The fit was performed with an orthogonal distance linear regression (ODR) on the logarithm of the data using scipy

python package [38]. The function finds the maximum likelihood and gives the estimated properties with their standard error, i.e. the error at one sigma interval. We accounted for the time error in the ODR fit and used all the 4 to 5 profiles measured at any given time. We chose a Pearson p-value of 1% to analyze the significance of the fit.

Figure 7 shows that the mean macroscopic force exhibits a clear power law trend. Only little deviations from the power law are observed, and the confidence intervals on the fitted parameters are rather small. The pre-factor F_{1h} ranges between 0.36 N and 1.22 N depending on the considered sample, and increases with specific surface area. Note that the values of F_{1h} for samples SSA18a and SSA18b, which are composed of similar grains, are very close but do not exactly coincide (see indicated errors). The exponent α_F is about 0.3 for all samples. Hence, it appears that the initial value of the macroscopic force F_{1h} depends on sample properties, while the power law exponent α_F is independent of the sample.

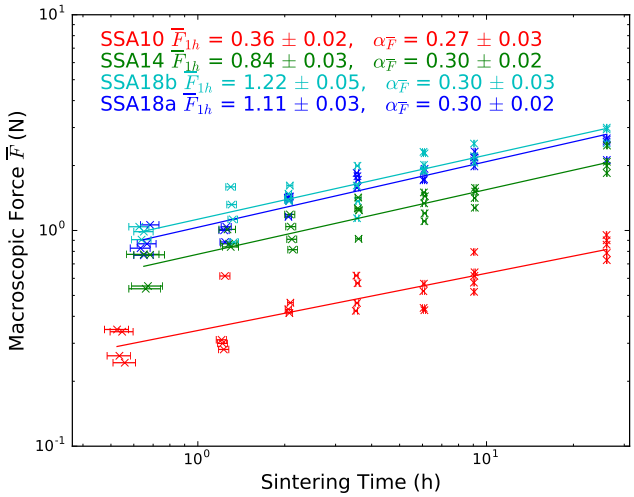

Figure 7: Evolution of the depth-averaged macroscopic force $\bar{F}$ with time for the different snow samples. The power law fits are shown by the solid lines, and the corresponding parameters are indicated in legend. The horizontal error bars represent the time error (around 10 minutes) due to non-instantaneous sample preparation.

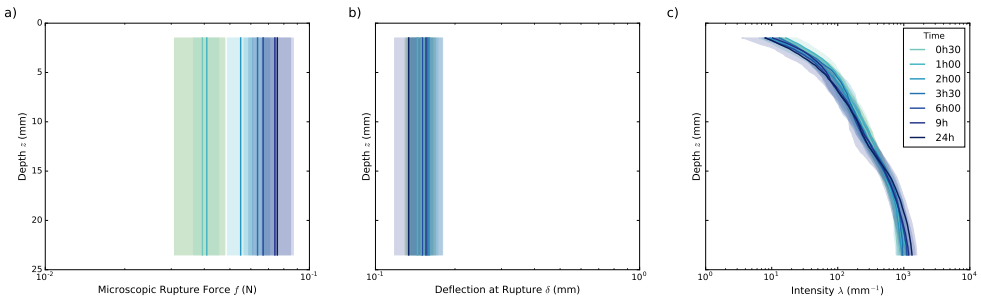

Figure 8: Vertical profiles of the micromechanical properties estimated by the NHPP model on sample SSA18a for different sintering times. The shaded area around the curves represents the standard deviation obtained for the different profiles at one sampling time.

3.3. Evolution of the micromechanical properties with time

Figure 8 shows the evolution with time, for sample SSA18a, of the micromechanical properties estimated by the NHPP analysis. Similar plots for the other samples are visible in Appendix C, Figs. C.12, C.13, C.14. The deflection δ and intensity λ_z do not show obvious changes with time (Figs. 8b, c). On the contrary, for the microscopic rupture force f, a clear increase with time is observed (Fig. 8a). Hence, according to the NHPP analysis, the evolution of the macroscopic force F (Fig. 6) with time is mainly due to the evolution of the microscopic rupture force, whereas its evolution with depth is explained by the vertical profile of the intensity. We recall that the NHPP model assumes that the microscopic rupture force is constant over depth, but not that intensity is constant over time.

As in Sect. 3.2, the time evolution of the micromechanical properties was approximated by fitting a power law : $X(t) = X_{1h}\,(t/t_{1h})^{\alpha_X}$, were X is either f, δ or $\overline{\lambda}$ (Figure 9). Again, a Pearson p-value of 1 % is used to assess the significance of the fits. The lines in Fig. 9 are dotted if the fit is not significant. Note that we consider here the averaged intensity over depth. Figures 9b,c confirm that the deflection and average intensity do not significantly change with time. The initial values of δ and $\overline{\lambda}$ are however dependent on sample properties. On the contrary, the microscopic rupture force f exhibits a clear power law trend. Again, only little deviations from the power law are observed, and the confidence intervals on the fit parameters are rather small. The pre-factor f_{1h} ranges from 0.05 N to 0.09 N and decreases when specific surface area increases. The value of f_{1h}

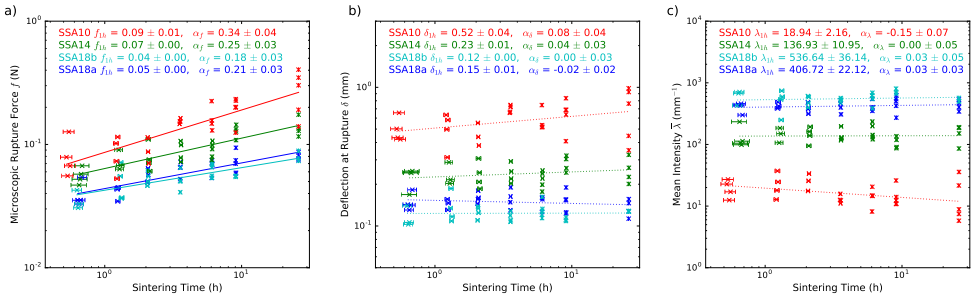

Figure 9: Time evolution of the micromechanical properties estimated by the NHPP model. The significant (resp. non-significant) power law fits are represented by the solid (resp. dotted) lines, with corresponding parameter indicated in legend. The horizontal error bars represent the time error (around 10 minutes) due to non instantaneous sample preparation.

for samples SSA18a and SSA18b, which were composed of similar snow grains, are very close. The exponent α_f ranges from 0.18 to 0.34, and appears to decrease with increasing specific surface area (or decreasing grain size). Hence, both the initial value and power law exponent of the microscopic rupture force are dependent on grain size.

4. Discussion

Due to a limited sample height of 35 mm, the presented μCPT profiles exhibit a non-stationary regime due to the progressive build-up of a compaction zone in front of the cone tip. To properly account for this feature and to estimate micromechanical properties from the μCPT profiles, we proposed a non-homogeneous Poisson shot noise model (NHPP). This approach follows up on the ideas of Löwe and Herwijnen [29], who described the fluctuating penetration force as a homogeneous Poisson shot noise process (HPP) with a single event described as an elastic-brittle rupture. We showed, under the assumption that the relative variations of intensity over an interval of size δ are small, that the analytical expressions for the cumulants and the correlation of the macroscopic force given by Löwe and Herwijnen [29] (Eq. 6 and 10 there) can be extended to a non homogeneous process, i.e. with an intensity λ_z varying with depth. This extension amounts to separate two spatial scales: the scale of the bond rupture characterized by δ and f, and the scale of the compaction zone that governs the evolution of λ_z. Using simulated force profiles with a linear evolving intensity (and properties close to those

of the snow samples used in this study), we showed that the NHPP model was able to retrieve accurate micromechanical properties (Fig. 4). In particular, on simulated profiles characterized by large variations of λ_z with depth, which mimic our measurements, the NHPP was more accurate than the HPP whose underlying assumptions are violated. On this type of profile, no window size, small enough to satisfy the assumption of constant parameters and large enough compared to the event spatial extent δ, can be found to correctly apply the HPP. The NHPP development was thus required to provide a robust estimates of the micromechanical parameters from the presented measurements. The main approximation of the NHPP model is the calculation of the first cumulant $\kappa_1(F)$. We approximate $\kappa_1(F)$ by its running mean over a window size of Δ_z=3 mm. Therefore, we assumed that the profile can be approximated by a linear evolution over such window sizes. A window of 3 mm was chosen as the best compromise between a sufficiently large window to get a better estimation of the parameter, and a sufficiently small window to assume the signal to evolve linearly over it. Comparing the HPP and NHPP on measured profiles showed clear differences between the estimated parameters by the two models (Fig. 5). Nevertheless, these differences become less pronounced for depths larger than 20 mm. In particular, the models estimate similar values of δ. The two models predict a similar evolution of f and λ with SSA but the estimated values are different for these depths. Thus, it would be interesting to compare the NHPP and HPP on thicker snow-samples, where the CZ can fully develop. In such a case, the NHPP and HPP would probably lead to similar estimates. Indeed, the NHPP is a generalization of the HPP, as it also includes zero-slope evolution of the intensity with depth. On a profile with no significant evolution of lambda, the NHPP would not provide any advantage over the standard HPP method but would perform as well as this method. Besides, it would be interesting to apply the NHPP on a whole profile of a snowpack with different snow layers. In particular, it may be still possible that a new compaction zone develops at each transition between a soft layer and a harder one, and not only at the snowpack surface.

We measured numerous μCPT profiles in quasi-homogeneous snow samples created in the laboratory and let to sinter during 24 hours at -10°C. The NHPP model was applied to these measurements. The derived micromechanical properties consistently distinguished the four snow samples prepared with different sieve sizes and varying mainly by grain size

(or SSA) and slightly by density. The largest values of microscopic rupture force f and deflection δ, and lowest values of intensity λ_z, were obtained for the largest grains and slightly lower densities than average (Fig. 5). Furthermore, only the microscopic rupture force was found to evolve significantly with time, while the parameters λ_z and δ remained essentially constant with time (Fig. 8). These results can be interpreted as a progressive growth of the bonds without any other structural changes in the snow.

The microstructural analysis thus exhibits a partition between the variations with depth (borne only by the intensity) and with time (borne only by the microscopic rupture force) of the macroscopic force profile. This observation is consistent with our expectation that the evolution over one day of the snow microstructure, excepted bond growth, would remain limited for samples composed of large rounded grains with a density around 500 kg m^{-3} and a SSA between 10 and 18 m^2 kg^{-1}. Hence, μCPT profiles with an appropriate statistical analysis indeed appear to provide relevant proxies of bond evolution during sintering. This point corroborates the finding of Herwijnen and Miller [19] who suggested that the SMP profile relates to bond scale processes, based on an agreement between the SMP mean force evolution and a physical bond-to-grain evolution model.

In previous studies, snow sintering was investigated at different scales, from the bond scale by recording the evolution of the bond size [e.g. 13, 14, 16] to the snowpack scale by recording the evolution of macroscopic mechanical properties such as shear or compression strength [e.g. 24, 26]. With the μCPT and the NHPP analysis, we were able to characterize the sintering process at two scales, through simultaneous records of the macroscopic penetration force F (Fig. 7) and of the microscopic rupture force f (Fig. 9a), a direct proxy for the bond size. Both F and f were shown to obey power laws with time, with similar exponents, namely $\alpha_F \approx 0.29$ (Fig. 7) and $\alpha_f \approx 0.27$ (Fig. 9a) (average values). Hence, the time-evolution of the macroscopic force F appears closely related to the evolution of the microscopic force f. Recall also that the intensity profile λ_z remains essentially constant over time, meaning that the progressive build-up of the tip-induced compaction zone is unaffected by sintering, at least in the considered dataset.

The obtained values of α_F are in agreement with previous studies at the macroscopic scale: Herwijnen [33] observed exponents between 0.2 and 0.3 for rounded grains with densities between about 350 to 400 kg m^{-3}. To compare the values of α_f to sintering

exponents involved in the evolution of bond size (a geometrical property), we can assume that f is proportional to $\sigma_{ice} \times r_b^2$ with σ_{ice} the strength of ice and r_b the bond radius. This assumption yields the relation $\alpha_f = 2\ \alpha_{rb}$ between the sintering exponents of f and bond radius r_b. According to Hobbs and Mason [14], the evolution of the bond-to-grain ratio for ice can be theoretically described by Eq.1 with $n = 5$ and $m = 3$, which yields $\alpha_{rb} = 1/5$. From experimental data, Hobbs and Mason [14] estimated sintering exponents of bond size between 0.16 and 0.24 at a temperature of -10°C. Kingery [12] measured exponents between 0.15 and 0.18 at temperatures of about -9.5°C and Kuroiwa [13] got an exponent of 0.2 at the same temperature. The sintering exponents of microscopic rupture force that we measured (between 0.18 and 0.34) are effectively higher than the ones theoretically obtained for bond size, but not by a factor of 2. Note, however, that all these studies considered ice spheres, while we worked with irregular grain shapes. Besides, Kuroiwa [13] and Hobbs and Mason [14] worked with much smaller ice spheres than ours, only Kingery [12] used ice spheres with a diameter between 0.6 and 1 mm. Moreover, deviations to the relation $\alpha_f = 2\ \alpha_{rb}$ can be expected if the stress distribution in a bond between grains is not homogeneous. The measured values of α_F do not change with SSA in the range between 10 and 18 $\mathrm{m^2\ kg^{-1}}$ and densities between 480 and 500 $\mathrm{kg\ m^{-3}}$. In contrast, the values of α_f were found to slightly increases with grain size, as observed by Hobbs and Mason [14]. Lastly, it is also noteworthy that a different behaviour with grain size was observed for the two pre-factors F_{1h} and f_{1h}: F_{1h} decreases, while f_{1h} increases, with increasing grain size. The behaviour of f_{1h} is consistent with classical sintering models predicting that bond radius should increase with grain size according to $r_b \propto r_g^{m/n}$ (see Eq. 1) [10].

5. Conclusions

We investigated snow sintering at -10°C by measuring numerous μCPT profiles conducted with a modified version of the SMP on samples characterized by different grain sizes during 24 hours. To analyze the fluctuating macroscopic force in terms of micromechanical properties, we extended the work of Löwe and Herwijnen [29] based on an homogeneous Poisson shot noise model. To this end, we also considered the penetration force as the result of the contribution of independent elastic-brittle failure events, but we relaxed

the assumption that the number of failure occurrences per penetration increment, i.e. the intensity, is constant over a certain analysis window. This non-homogeneous Poisson shot noise model is able to characterize the snow micromechanical properties of a homogeneous snow layer even if the cone penetration test is in a transient state, due to the progressive formation of a compaction zone in front of the cone tip. On simulated profiles with prescribed spatial variations of the intensity, the model provided accurate estimates of the micromechanical properties. On the measured μCPT profiles, the model decomposed the evolution of the macroscopic force with depth and time as a constant vertical intensity profile and a time evolution of the microscopic rupture force. This partition is consistent with the absence of evolution of the grain themselves (e.g. shape) in the tested samples and bond growth with sintering. The power law exponents for the macroscopic and microscopic rupture forces ($\alpha_F \approx 0.29$ and $\alpha_f \approx 0.27$, respectively) were very close and in line with previous studies. In addition, the analysis of α_f revealed a higher sintering rate for the largest grains and the pre-factor f_{1h} of the power law was shown to increase with grain size, which is in line with the theory of bond growth. However, the limited number (four) of tested samples did not enable us to provide quantitative relations between grain size and sintering rate. Our analysis nevertheless showed that micro-cone penetration tests, combined with an appropriate analysis method enables a fast and simple characterization of the snow structure. It would be thus possible to investigate the snow evolution with metamorphism on snow samples spanning a wider range of microstructural patterns.

The HPP and NHPP models could be evaluated with micro-tomographical measurements, as mentioned by Löwe and Herwijnen [29]. Indeed, micro-tomography can be used to provide direct estimates of microstructural properties derived from μCPT. In particular, the contact force f could be related to the bond size derived from tomographic data using the concept of the minimum cut surface [39]. We are currently working on combined μCPT and micro tomographical measurements. This data includes high-resolution measurements of the snow microstructure before and after a μCPT. It could provide a direct evaluation of the HPP and NHPP models and could give new insights on the deformation mechanisms occurring at the cone tip.

6. Acknowledgements

We thank S. Morin, N. Eckert, L. Arnaud, C. Geindreau and F. Flin for fruitful discussions. CNRM/CEN is part of LabEX OSUG@2020 (ANR10 LABX56). Irstea is part of LabEX TEC21 (ANR11 LABX30). This work was partly supported by the European Space Agency under ESTEC Contract No. 4000112698/14/NL/LvH.

Appendix A. Evaluation of modified SMP

In this appendix, we compare the measured force signal of the original SMP and the modified version used in our study. For simplicity, we denote the measured profiles as followed: μCPT profiles are measured with the modified SMP and SMP profiles are measured with the original setup. Fig. A.10 shows two couples of SMP and μCPT profiles, which were measured within a distance of about 5 cm in one snow sample. The snow sample was made of large rounded grains, with a density of about 480$\pm$20 kg m^{-3} and a SSA of 14.38$\pm$0.9 m^2 kg^{-1}. The maximal depth of the SMP profiles is the height of the snow sample. Small differences in the sample height are due to the sieving procedure. Comparing the first 35 mm of the profiles, we notice a higher force for the SMP profiles, than for the μCPT profiles. A clear difference between the profiles can be observed for depth larger than about 5 mm of penetration, where the rod touches in the snow. Above, no obvious difference is visible.

A more quantitative analysis was done by computing the mean and standard deviation on the first 5 and 25 mm of the profile. At a depth of about 5 mm, the SMP rod reaches the snow surface and its CZ could influence the measured signal. To get an information of the fluctuations of the force profile, we computed the mean of the macroscopic force, its standard deviation, and its correlation length ($C(0)/C'(0)$, with the two point correlation function C, [29]) over the two depth intervals. The results of these computations are shown in Tab. A.2. For the computed properties over the first 5 mm, we observe a good agreement between the SMP and μCPT profiles. In contrast to this, the analysis over 25 mm depth shows obvious differences between both measuring methods. Here, a clear influence due to the indentation of the SMP rod is observed. These results show that the extension seems to have no influence on the force sensor, as there were no remarkable differences in the signals for the depths where the rod did not touch the snow. In contrast,

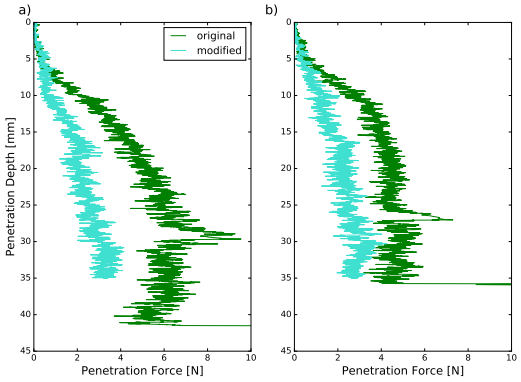

Figure A.10: Penetration profiles measured with the original setup (SMP) and the modified setup (μCPT). The comparison was repeated for two couples of profiles (a and b). In one couple, the profiles were measured close to each other.

Table A.2: Statistical calculations on the profiles of the SMP and μCPT measurements. The calculations were done over two different windows, the first 5 and the first 25 mm of the profile.

window	mean				standard deviation				C(0)/C'(0)			
(mm)	SMP		μCPT		SMP		μCPT		SMP		μCPT	
5	0.13	0.22	0.17	0.16	0.13	0.18	0.17	0.15	0.067	0.078	0.077	0.094
25	2.94	2.82	1.37	1.38	2.14	1.71	0.88	0.89	0.15	0.38	0.10	0.11

large differences in the measured profile were observed when the rod indented the snow, which might be enhanced by the limited depth of our samples.

Appendix B. Mathematical developments

In this appendix, we prove Eq. 4 and explain why $\widetilde{F}$ can be considered as stationary.

The general equation for the cumulant κ_n of order n of a signal, which can be described by a non-homogeneous shot noise process, is given by Campbell's theorem [e.g. 40]:

$$\kappa_n(z) = \int_{-\infty}^{\infty} \lambda_z(\tau) f_z^n(z-\tau) d\tau \tag{B.1}$$

Furthermore, the auto-correlation C of the signal is given by [e.g. 40]:

$$C(z, z+u) = \int_{-\infty}^{\infty} \lambda_z(\tau) f_z(z-\tau) f_z(z+u-\tau) d\tau \tag{B.2}$$

We now express $\lambda_z(z)$ a polynomial function $\sum_{m=0}^{M} a_m z^m$. Inserting the expression $f_z(z) = f/\delta \times \theta(z) \times \theta(\delta - z)$, where θ is the Heaviside function, into Eqs. B.1 and B.2, we obtain

$$\kappa_n(z) = f^n \delta \sum_{l=0}^{M} \left[\frac{\delta^l (-1)^l}{(l+n+1)l!} \frac{d^l}{dz^l} \left(\sum_{m=0}^{M} a_m z^m \right) \right], n = 1, 2 \tag{B.3}$$

$$C(z, z+u) = \frac{f^2}{\delta^2} \sum_{l=0}^{M} \left[(-1)^l \left(\frac{u(\delta-u)^{l+2}}{(l+2)l!} + \frac{(\delta-u)^{l+3}}{(l+3)l!} \right) \frac{d^l}{dz^l} \left(\sum_{m=0}^{M} a_m z^m \right) \right] \tag{B.4}$$

If the variations of the intensity over an interval of the size of δ are small compared to the mean intensity, all the terms with $l \geq 1$ in the above summation can be neglected. Equation B.4 then simplifies to:

$$\kappa_n(z) = \frac{f^n \delta \lambda_z(z)}{n+1} \quad \text{and} \quad C(z, z+r, |r| < \delta) = f^2 \delta \lambda_z(z) \left(\frac{1}{3} - \frac{1}{2}\frac{|r|}{\delta} + \frac{1}{6}\frac{|r|^3}{\delta^3} \right). \tag{B.5}$$

Computing the cumulants and the correlation function of $\widetilde{F} = (F - \kappa_1(F))/\kappa_1(F)^{1/2}$ with Eq. B.5, it appears that they are independent of z, which indicates that $\widetilde{F}$ is stationary.

Appendix C. Time evolution of the macroscopic and microscopic property profiles

This appendix provides the equivalents of Figs. 6 and 8 (corresponding to sample SSA18a above) for samples SSA18b, SSA14 and SSA10.

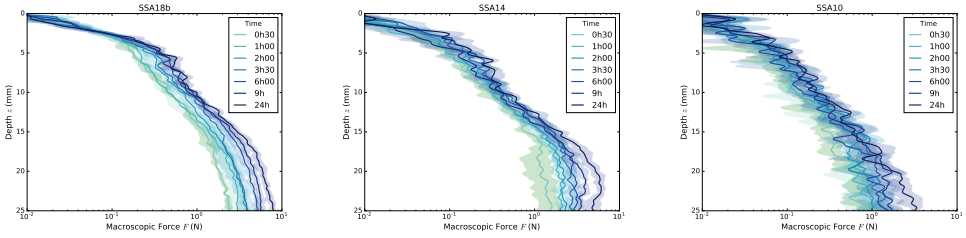

Figure C.11: Evolution of the vertical profiles of the macroscopic force with time, measured on the samples SSA18b, SSA14 and SSA10.

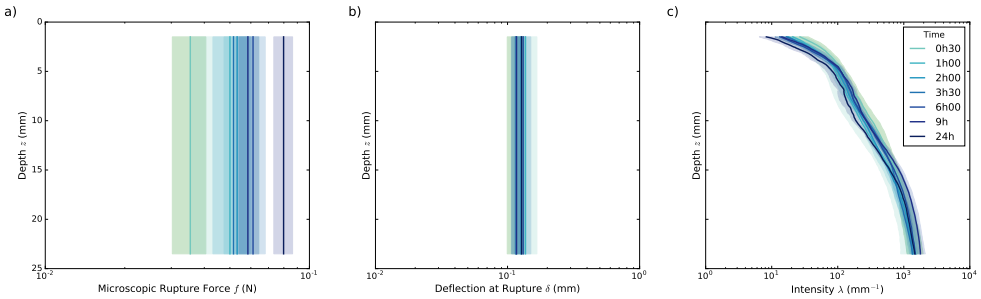

Figure C.12: Time evolution of the profiles of the micromechanical properties estimated by the NHPP model on sample SSA18b. The shaded area around the curves represents the standard deviation obtained for the different profiles at one sampling time.

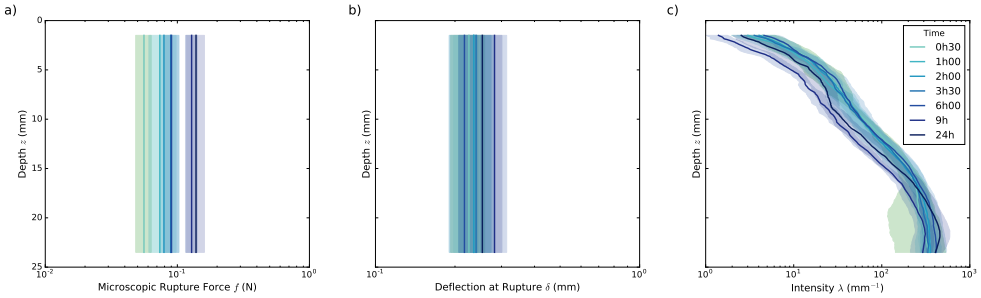

Figure C.13: Time evolution of the profiles of the micromechanical properties estimated by the NHPP model on sample SSA14. The shaded area around the curves represents the standard deviation obtained for the different profiles at one sampling time.

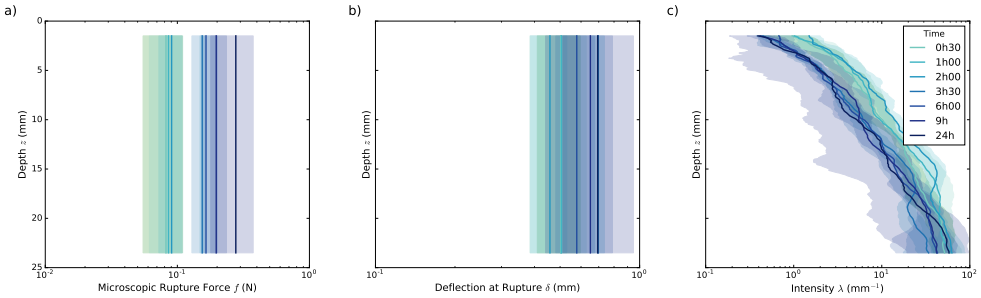

Figure C.14: Time evolution of the profiles of the micromechanical properties estimated by the NHPP model on sample SSA10. The shaded area around the curves represents the standard deviation obtained for the different profiles at one sampling time.

[1] J. Blackford, Sintering and microstructure of ice: a review, J. Phys. D: Appl. Phys. 40 (2007) R355–R385.

[2] H. Gubler, Determination of the mean number of bonds per snow grain and of the dependence of the tensile strength of snow on stereological parameters, J. Glaciol. 20 (1978) 329–341.

[3] I. Reiweger, J. Schweizer, J. Dual, H. J. Herrmann, Modelling snow failure with a fibre bundle model, J. Glaciol. 55 (2009) 997–1002.

[4] D. Szabo, M. Schneebeli, Subsecound sintering of ice, Appl. Phys. Lett. 90 (2007).

[5] K. Birkeland, K. Kronholm, S. Logan, J. Schweizer, Field measurements of sintering after fracture of snowpack weak layers, Geophys. Res. Lett. 33 (2006).

[6] S. C. Colbeck, A review of sintering in seasonal snow, CRREL Report, US Army Corps of Engineers, Cold Regions Research & Engineering Laboratory (1997) 97–10.

[7] A. Gow, Time - temperature dependence of sintering in perennial isothermal snowpacks, Snow Mechanics 114 (1975) 25–41.

[8] D. M. McClung, The critical size of macroscopic imperfections in dry snow slab avalanche initiation, J. Geophys. Res 116 (2011) F03003.

[9] M. Fauve, H. Rhyner, M. Schneebeli, Préparation et entretien des pistes. Manuel pour le praticien., Davos, Institut fédérale pour l'étude de la neige et des avalanches, 2002.

[10] G. C. Kuczynski, Self-diffusion in sintering of metallic particles, Transactions of AIME 185 (1949) 169–178.

[11] J. Frenkel, Viscous flow of crystalline bodies under the action of surface tension, Journal of Physics U.S.S.R. 9 (1945) 385–431.

[12] W. D. Kingery, Regelation, surface diffusion, and ice sintering, J. Appl. Phys. 31 (1960) 833–838.

[13] D. Kuroiwa, A study of ice sintering, Tellus 13 (1961).

[14] P. V. Hobbs, B. J. Mason, The sintering and adhesion of ice, Philos. Mag. 9 (1964) 181–197.

[15] N. Maeno, T. Ebinuma, Pressure sintering of ice and its implication to the densification of snow at polar glaciers and ice sheets, J. Phys. Chem. 87 (1983) 4103–4110.

[16] S. Chen, I. Baker, Structural evolution during ice-sphere sintering, Hydrol. Process. (2010).

[17] M. Mellor, A review of basic snow mechanics, IAHS Publication 114 (1975) 251–291.

[18] D. M. McClung, P. Schaerer, The Avalanche Handbook, Mountaineers, Seattle, Wash, 3rd edition, 2006.

[19] A. Herwijnen, D. A. Miller, Experimental and numerical investigation of the sintering rate of snow, J. Glaciol. 59 (2013) 1–6.

[20] T. Kaempfer, M. Schneebeli, Observation of isothermal metamorphism of new snow and interpretation as a sintering process, Journal of Geophysical Research (Atmospheres) 112 (2007) 24101–.

[21] X. Wang, I. Baker, Observation of the microstructural evolution of snow under uniaxial compression using x-ray computed microtomography, Journal of Geophysical Research: Atmospheres 118 (2013) 12,371–12,382.

[22] S. Schleef, H. Löwe, X-ray microtomography analysis of isothermal densification of new snow under external mechanical stress, J. Glaciol. 59 (2013) 233–243.

[23] C. Chandel, P. K. Srivastava, P. Mahajan, Micromechanical analysis of deformation of snow using X-ray tomography, Cold Regions Science and Technology 101 (2014) 14 – 23.

[24] R. O. Ramseier, G. W. Sander, Sintering of snow as a function of temperature, in: Symposium at Davos 1965 - Scientific Aspects of Snow and Ice Avalanches, 5-10 April 1965, 69, Int. Assoc. of Sci. Hydrol., Geneva, Switzerland, Publ.,, 1966, pp. 119–127.

[25] H. Matsushita, M. Matsuzawa, O. Abe, The influences of temperature and normal load on the shear strength of snow consisting of precipitation particles, Ann. Glaciol 53 (2012) 31–38.

[26] V. d. Montmollin, Shear test on snow explained by fast metamorphism, J. Glaciol. 28 (1982) 187–198.

[27] M. Schneebeli, J. Johnson, A constant-speed penetrometer for high-resolution snow stratigraphy, Ann. Glaciol 26 (1998) 107–111.

[28] E. A. Podolskiy, M. Barbero, F. Barpi, G. Chambon, M. Borri-Brunetto, O. Pallara, B. Frigo, B. Chiaia, M. N. 1, Healing of snow surface-to-surface contacts by isothermal sintering, The Cryosphere 8 (2014) 1651–1659.

[29] H. Löwe, A. Herwijnen, A Poisson shot noise model for micro-penetration of snow, Cold Reg. Sci. Technol. 70 (2012) 62–70.

[30] C. Fierz, R. L. Armstrong, Y. Durand, P. Etchevers, E. Greene, D. M. McClung, K. Nishimura, P. K. Satyawali, S. A. Sokratov, The international classification for seasonal snow on the ground, Tech. Doc. Hydrol., 83, UNESCO, Paris (2009).

[31] J.-C. Gallet, F. Domine, C. S. Zender, G. Picard, Measurement of the specific surface area of snow using infrared reflectance in an integrating sphere at 1310 and 1550 nm, The Cryosphere 3 (2009) 167–182.

[32] A. LeBaron, D. Miller, A. van Herwijnen, Measurements of the deformation zone around a split-axis snow micropenetrometer tip, Cold Regions Science and Technology 97 (2014) 90 – 96.

[33] A. V. Herwijnen, Experimental analysis of snow micropenetrometer (SMP) cone penetration in homogeneous snow layers, Can. Geotech. J. 50 (2013) 1044–1054.

[34] J. Johnson, M. Schneebeli, Characterizing the microstructural and micromechanical properties of snow, Cold Reg. Sci. Technol. 30 (1999) 91–100.

[35] H.-P. Marshall, J. Johnson, Accurate inversion of high-resolution snow penetrometer signals for microstructural and micromechanical properties, J. Geophys. Res. 114 (2009) F04016.

609 [36] M. Proksch, H. Löwe, M. Schneebeli, Density, specific surface area, and correlation
610 length of snow measured by high-resolution penetrometry, Journal of Geophysical
611 Research: Earth Surface 120 (2015) 346–362.

612 [37] S. Ruiz, A. Capelli, A. van Herwijnen, M. Schneebeli, D. Or, Continuum cavity
613 expansion and discrete micromechanical models for inferring macroscopic snow me-
614 chanical properties from cone penetration data, Geophys. Res. Lett. 44 (2017).

615 [38] P. T. Boggs, J. E. Rogers, Orthogonal distance regression, in: C. Mathematics (Ed.),
616 Statistical analysis of measurement error models and applications: proceedings of the
617 AMS-IMS-SIAM joint summer research conference held June 10-16, 1989, 112, p. 186.

618 [39] P. Hagenmuller, N. Calonne, G. Chambon, F. Flin, C. Geindreau, M. Naaim, Char-
619 acterization of the snow microstructural bonding system through the minimum cut
620 density, Cold Regions Science and Technology 108 (2014) 72 – 79.

621 [40] A. Papoulis, Probability, Random Variables, and Stochastic Processes, McGraw-Hill,
622 3rd ed. edition, 1991.